



An Optimized Method for Terrain Reconstruction Based on Descent Images

Xu Xinchao^{1,2*}, Zheng Zhenzhen¹, Xu Aigong¹ & Liu Shaochuang²

¹School of Gematics, Liaoning Technical University, LiaonngFuxin 123000, China

²Institute of Remote Sensing and Digital Earth,
Chinese Academy of Sciences, Beijing 100101, China

Email: xu_xinchao@163.com

Abstract. An optimization method is proposed to perform high-accuracy terrain reconstruction of the landing area of Chang'e III. First, feature matching is conducted using geometric model constraints. Then, the initial terrain is obtained and the initial normal vector of each point is solved on the basis of the initial terrain. By changing the vector around the initial normal vector in small steps a set of new vectors is obtained. By combining these vectors with the direction of light and camera, the functions are set up on the basis of a surface reflection model. Then, a series of gray values is derived by solving the equations. The new optimized vector is recorded when the obtained gray value is closest to the corresponding pixel. Finally, the optimized terrain is obtained after iteration of the vector field. Experiments were conducted using the laboratory images and descent images of Chang'e III. The results showed that the performance of the proposed method was better than that of the classical feature matching method. It can provide a reference for terrain reconstruction of the landing area in subsequent moon exploration missions.

Keywords: *Chang'e III; descent images; feature point extraction; geometric constraint; terrain reconstruction.*

1 Introduction

In lunar exploration, high-precision terrain reconstruction of the landing area has significance for achieving the scientific objectives of future projects and is important for safety and efficient path planning of the rover [1]. The Chang'e II detector acquired a large number of lunar images and other information in previous lunar exploration projects. Digital orthophoto maps with 1.5 m resolution and digital elevation models with 4 m resolution are currently being produced using the existing images captured by the Chang'e II satellite [2-4]. However, a terrain reconstruction with this accuracy can only be used for macro scientific investigation and cannot be used for path planning of the rover of Chang'e III [5]. The navigation cameras attached to the Chang'e III rover have a high resolution and can provide the basis for high-precision terrain reconstruction. However, the use of navigation cameras was not conducive to

the overall plan because of its small coverage. A total of 4,672 high-resolution images were acquired during the descent of Chang'e III [6]. These images are important for the subsequent reconstruction of the landing area.

Binocular stereo technology in computer vision and three-dimensional (3D) reconstruction technology in the field of photogrammetry are considered to be more mature. Ni improved the SIFT (scale-invariant feature transform) algorithm to register ultrasound volumes acquired globally from dedicated ultrasound probes [7]. Bulatov assumed that camera matrices and a sparse set of 3D points are available and computed dense 3D point clouds from a sequential set of images [8]. Xue eliminated match-related value noise by using a Gaussian filter and utilized the smooth-constraint match cost function to smoothen discontinuity disparity areas [9]. Shin progressively updated the matching weight for each pixel by using a relaxation labeling technique and improved matching performance [10]. Ahmadabadian compared the accuracy of four topical surface dense matching methods, which included two versions of semi-global matching, namely MicMac and PMVS (patch-based multi-view stereo) [11]. Dellepiane presented a methodology for effective acquisition and data processing and 3D data integration in an open-source mesh processing tool [12]. Meng proposed a homography-based depth recovery method for descent images [13]. Joglekar presented a feature matching algorithm for the dense matching technique based on a probabilistic neural network [14]. Nebiker completed the reconstruction of historical aerial imagery and the subsequent analysis of settlement change [15]. Stentoumis proposed a local stereo method with high computational efficiency and achieved accurate 3D reconstruction under various scenarios [16]. Meng proposed a new matching method based on best seed propagation considering neighborhood disparity constraints [17]. Koutsoudisa enhanced the reconstruction performance of featureless surfaces by using noise function-based patterns [18]. Liu used the complementary characteristics of stereo matching and depth sensing to improve depth estimation [19]. Chen transformed the SIFT features to binary representations and significantly decreased the complexity of distance calculation [20].

The aforementioned methods exhibited a good effect on 3D reconstruction. However, the descent images were captured on a vertical photographic baseline and moon images are characterized by texture repetition and/or lack of texture. Therefore, mismatches were still observed in the dense matching results and the reconstructed terrain exhibited low reliability and poor accuracy. We can obtain more feature points when the threshold is lowered but more mismatches will occur. A higher threshold will lead to less matching points and a relatively rough reconstruction result. Hence, a high-precision 3D terrain reconstruction algorithm suitable for descent images is necessary.

2 Description of the Proposed Algorithm

Given that the terrain obtained by using traditional dense matching and feature matching cannot meet the needs of the scientific expedition mission of Chang'e III, an optimization method is proposed. Optimization of feature matching is conducted by using geometric model constraints after which the initial terrain is obtained. The normal vector of each point is solved on the basis of the initial terrain. Then, the reflection model of the object surface is used to optimize the normal vector. Finally, the optimized terrain reconstruction is obtained. The proposed method consists of four main steps, namely feature extraction, feature matching under the geometric model constraints, initial terrain construction, and normal vector optimization.

2.1 Forstner Feature Point Extraction

A feature point extraction method with high precision, such as the Forstner algorithm, should be selected to improve the accuracy of the reconstruction. The main process of this method is divided into three steps: first, the Robert's gradient of each pixel is calculated; then, the gray covariance matrix of a window (e.g. 5×5), which takes the current pixel as the center, is calculated; and finally, the points, which are denoted by small error ellipses that are close to a circle, are used as feature points [21]. The detailed steps of the algorithm are as follows:

1. Assuming that $I_{m,n}$ is the gray value of the pixel (m,n) , the gray gradient of the pixel can be calculated according to Eq. (1), as follows:

$$\begin{cases} G_x = \partial I / \partial x = I_{m+1,n+1} - I_{m,n} \\ G_y = \partial I / \partial y = I_{m,n+1} - I_{m+1,n} \end{cases} \quad (1)$$

2. Taking the current pixel (m,n) as the center of the window, we can derive $k = \text{INT}(W/2)$ according to the designed window size W . Then, the gray covariance matrix N can be computed as follows:

$$N = \begin{bmatrix} \sum G_x^2 & \sum G_x G_y \\ \sum G_y G_x & \sum G_y^2 \end{bmatrix} \quad (2)$$

where:

$$\sum G_x = \sum_{i=m-k}^{m+k-1} \sum_{j=n-k}^{n+k-1} (I_{i+1,j+1} - I_{i,j}) \quad (3)$$

$$\sum G_y = \sum_{i=m-k}^{m+k-1} \sum_{j=n-k}^{n+k-1} (I_{i,j+1} - I_{i,j}) \quad (4)$$

3. Parameters q and ω are calculated according to Eqs. (5) and (6), as follows:

$$q = 4 \text{Det}N / (\text{tr}N)^2 \quad (5)$$

$$\omega = \text{Det}N / \text{tr}N \quad (6)$$

where $\text{Det}N$ is the determinant of matrix N and $\text{tr}N$ represents the trace of matrix N .

4. Candidate point determination. If the values of q and ω are larger than a given threshold, then the pixel is considered the feature point. The threshold is an empirical value. Its value is determined by calculating Eq. (7), as follows:

$$\left. \begin{array}{l} T_q = 0.5 \sim 0.75 \\ T_\omega = \left\{ \begin{array}{l} f \bar{\omega} \quad (f = 0.5 \sim 1.5) \\ 5 \cdot \omega_c \end{array} \right\} \end{array} \right\} \quad (7)$$

where $\bar{\omega}$ is the mean value of weight and ω_c represents the median weight.

A quasi-dense match is needed. As such, when a feature point is finally selected, the window extreme point selection process in traditional methods is no longer conducted. Thus, the extracted points can reflect the terrain features better.

2.2 Matching Constraint

Given that lunar soil is composed of a single component, there are more texture-deficient or texture-repeat regions. Therefore, more mismatches occur in dense matching using traditional methods and the terrain reconstruction obtained by feature matching is relatively rough. In this study, we used descent images to reconstruct the terrain of a lunar landing area. Therefore, the matching constraint was investigated on the basis of a geometric model of the landing process. Descent images of Chang'e III are captured vertically at a height of 100 m or less. Figure 1 shows a schematic diagram of the descent process during which the images are captured.

We assume that the exterior orientation elements of the descent image are $(X_s, Y_s, Z_s, \varphi, \omega, k)$, where (X_s, Y_s, Z_s) are the position factors, (φ) is the tilt angle of the image, (ω) is the slant angle of the image, and (k) is the rotation angle of the image. (φ) and (ω) between the adjacent descent images can be

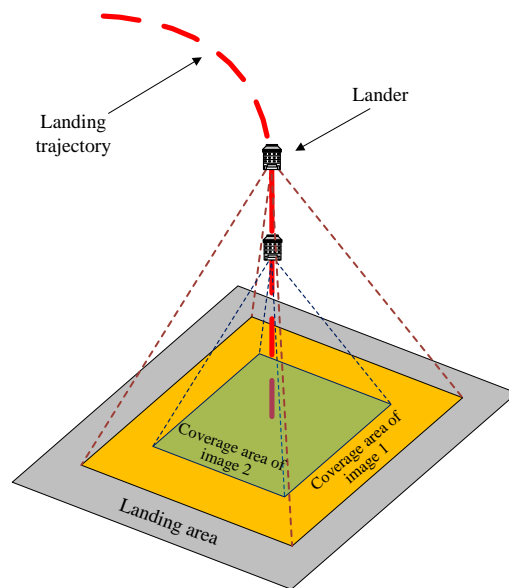


Figure 1 Schematic diagram of the descent image capture process.

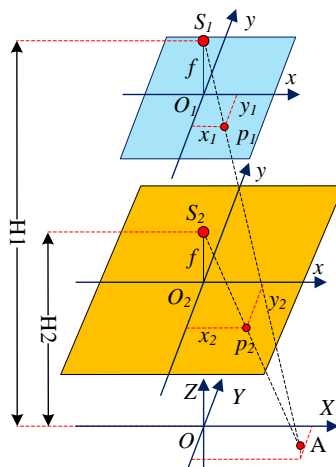


Figure 2 Relative position of descent images.

acquired by using the relative orientation and have a value of 0. A small rotation angle (k) also exists. For 3D reconstruction, we must obtain a high-precision matching point. Therefore, the relative orientation of the two descent images for terrain reconstruction is corrected using the traditional distortion correction

method. Then, the images are corrected according to the relative orientation parameters such that only the vertical displacement of the two images exists after the correction process. Figure 2 shows a schematic diagram of the geometric model of the two corrected images, where O_1 and O_2 are the main points of the two images, H_1 and H_2 are the height of captured images, A is an arbitrary point on the moon surface, and p_1 and p_2 are the corresponding matching points of the two descent images. The coordinates of A , p_1 , and p_2 are (X, Y, Z) , (x_1, y_1) , and (x_2, y_2) , respectively.

The focal length of the landing camera is assumed to be f . Eqs. (8) and (9) can be obtained from Figure 2, as follows:

$$\frac{f}{H_1 - Z} = \frac{x_1}{X} = \frac{y_1}{Y} \quad (8)$$

$$\frac{f}{H_2 - Z} = \frac{x_2}{X} = \frac{y_2}{Y} \quad (9)$$

By subtracting Eq. (9) from Eq. (8), the relationship of coordinate x between the matching points can be obtained, as follows:

$$x_2 = \frac{x_1 \cdot X \cdot f}{x_1 \cdot \Delta H + f \cdot X} \quad (10)$$

where $\Delta H = H_2 - H_1$.

In the same manner, the relationship of coordinate y between the matching points can be obtained, as follows:

$$y_2 = \frac{y_1 \cdot Y \cdot f}{y_1 \cdot \Delta H + f \cdot Y} \quad (11)$$

By using Formula (10) we can obtain the ideal matching point coordinates of the extracted feature points, as discussed in Section 1.1. Other points in the image can be solved in a similar manner.

However, image distortion cannot be eliminated completely. A certain size window, which takes the ideal coordinates obtained from Eqs. (10) and (11) as the center, is defined to derive the optimal matching point. Then, the best matching points are obtained from this window.

2.3 Construction of Initial Terrain

As the tilt angle (φ) and slant angle (ω) do not exist in the vertical descent process, we can assume that the exterior orientation elements of descent image 1 are $(X_{s1}, Y_{s1}, Z_{s1}, 0, 0, k_1)$; the exterior orientation elements of descent image 2 are $(X_{s2}, Y_{s2}, Z_{s2}, 0, 0, k_2)$; the pixel coordinates of points p_1 and p_2 presented in Section 1.2 are (x_1, y_1) , and (x_2, y_2) , respectively; and the coordinates of ground point A to be solved are (X, Y, Z) . The equations based on the classical collinear equation can be established as follows:

$$\begin{aligned}
 x_1 &= -f \frac{\cos k_1 (X - X_{s1}) + \sin k_1 (Y - Y_{s1})}{(Z - Z_{s1})} \\
 y_1 &= -f \frac{-\sin k_1 (X - X_{s1}) + \cos k_1 (Y - Y_{s1})}{(Z - Z_{s1})} \\
 x_2 &= -f \frac{\cos k_2 (X - X_{s2}) + \sin k_2 (Y - Y_{s2})}{(Z - Z_{s2})} \\
 y_2 &= -f \frac{-\sin k_2 (X - X_{s2}) + \cos k_2 (Y - Y_{s2})}{(Z - Z_{s2})}
 \end{aligned} \tag{12}$$

Notably, Eq. (12) is nonlinear and needs to be linearized first. The coordinates (X, Y, Z) of the matching points can be obtained by using the least square solution of the linearized equation. By incorporating the pixel coordinates of points p_1 and p_2 into Eq. (12), the 3D coordinates of the feature points can be obtained. Finally, the initial 3D terrain can be established using the 3D coordinates of these points.

2.4 Terrain Optimization

Any object surface can be described by a specific reflection model. Out of many proposed reflection models, the Lommel-Seeliger reflection model is considered to be the closest to the actual reflection situation on the moon [22]. Therefore, we use the Lommel-Seeliger model to optimize the normal vectors of the terrain points and to achieve the purpose of optimizing the final terrain. In the Lommel-Seeliger reflection model, the intensity of the light is not only related to the incident angle of the sun but also to the direction of the observer. The final model is described as a combination of the incidence and observation angles [23]. The Lommel-Seeliger normalization function used in this study can be expressed as follows:

$$I(x, y) = \frac{\omega}{4} \cdot \frac{\cos l}{\cos l + \cos e} \tag{13}$$

where $I(x, y)$ is the gray value of pixel (x, y) , ω is the surface reflectivity, $\cos l$ is the cosine of the incidence angle of light, and $\cos e$ is the cosine of the observation angle, namely the angle between the camera direction and the normal vector.

A contour map of the landing zone can be drawn according to the initial topography presented in Section 1.3. The initial normal vector $N(x, y, z)$ of the point corresponding to each pixel can also be solved. Subsequently, the initial normal vector is converted into a gradient form, namely $N(p, q, -1)$. By incorporating the light direction, initial normal vector, reflectivity, and observation direction into Eq. (13), we can derive a new pixel gray value. Given the difference between the initial normal vector and the real normal vector, a certain difference between the obtained gray value and the gray value of the original image also exists. The real normal vector must exist in a small range around the initial normal vector. Therefore, assuming that $k = q/p$, with k changing between $(k - \sigma, k + \sigma)$, a series of new gray values can be obtained according to Eq. (13). Finally, k can be determined when the obtained gray values are closest to the gray value in the image, which is the best direction to show the actual situation. Traversing the entire image, final optimization of the terrain is obtained after all the normal vectors are optimized.

2.5 Algorithm Implementation

The main processes of our algorithm are as follows: first, by combining the feature point extraction method with higher accuracy, feature points in the descent image with a small coverage are extracted. Then, according to the matching constraint, the matching points are obtained. The 3D coordinates of the matching points under the lander centroid coordinate system can be solved and combined with the exterior orientation elements of the image. Based on the Lommel-Seeliger reflection model, the vectors of each point can be optimized. Finally, terrain optimization is completed. The details of these processes are as follows:

1. Two images are selected from the descent images, and the direction of illumination and the exterior orientation elements corresponding to the images are obtained on the basis of the recording time.
2. An image with a small coverage is chosen from the two images selected in step 1. Then, feature point extraction is conducted using the high-precision method presented in Section 1.1. The feature points should be extracted as much as possible to ensure that the initial terrain exhibits a better reaction to the real terrain.
3. By combining the exterior orientation elements, the image pose is adjusted. Then, by substituting the feature point coordinates obtained in step 2 into

Eqs. (10) and (11), the ideal matching point coordinates in the other images are obtained. Given the presence of errors, a window is designed, which takes the ideal pixel as the center. The size of the window is 7×7 . In this window, the best matching point coordinates are determined using the correlation coefficient method. This process is repeated until all the best matching pixels for all the feature points are obtained.

4. According to the linearized Eq. (12) combined with the external orientation elements, the ground coordinate of a matching point is obtained using the least square method. The ground coordinates of all the matching points can be solved in the same manner. Finally, the initial terrain of the coverage area is constructed by using these ground point coordinates.
5. The normal vectors of all the ground points corresponding to each pixel under gradient form are solved throughout the initial terrain. By incorporating the obtained vectors, illumination direction, and exterior orientation elements into Eq. (13), a new gray value corresponding to each pixel can be derived.
6. Taking one point as example. Assuming $k = q/p$, with k varying between $(k - \sigma, k + \sigma)$ in certain small steps, a series of vectors for the current point can be obtained. Then, by incorporating the vectors, pixel coordinate corresponding to the point, illumination direction, and exterior orientation elements into Eq. (13), a set of gray values can be obtained. k is recorded when the calculated gray value is closest to the value of the corresponding pixel in the original image. Then, the optimized normal vector of the pixel is obtained, namely, $(p, kp, -1)$. All the vectors of the other points can be optimized in the same manner. Finally, terrain optimization is achieved by iteration of the optimized vector field.

3 Experimental Results and Discussion

Laboratory images were used to assess the accuracy of the proposed algorithm. The effects of the 3D reconstruction of the actual landing images of Chang'e III were also tested.

3.1 Laboratory Images

The landing process was simulated in the laboratory. The experiments were conducted using the obtained images to verify the accuracy of the overall algorithm. The light directions were $(1, 0.1, 0.7)$. The simulated descent images 1 to 4 are shown in Figures 3(a), 3(b), 3(c), and 3(d), respectively. Image 1 was taken at a height of 6.2 m, Image 2 at 7.5 m, Image 3 at 3.6 m, and Image 4 at 4.8 m. A FARO 3D laser scanner was used to scan the simulated surface in the laboratory with an interval between scan points of 0.5 cm. By taking the scan results as the truth, the accuracy of the proposed method was tested.

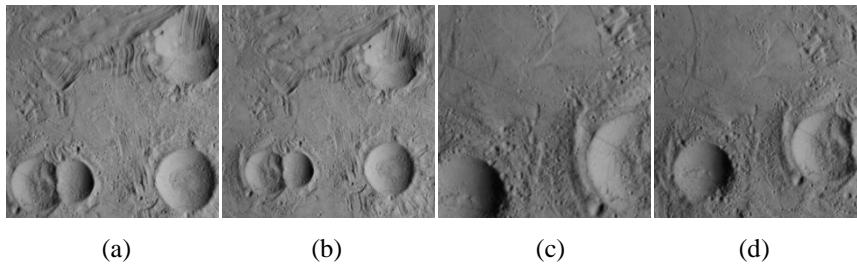


Figure 3 Laboratory images.

The coverage areas of Images 1 and 3 are small. Therefore, feature point extraction using the Forstner method was first conducted on these two images. Then, the matching points in Images 2 and 4 corresponding to the extracted feature points were obtained by using the proposed matching constraint. To facilitate viewing, the sparse matching results are displayed in Figure 4. Figure 4(a) shows the matching result of descent Images 1 and 2. Figure 4(b) shows the matching result of descent Images 3 and 4.

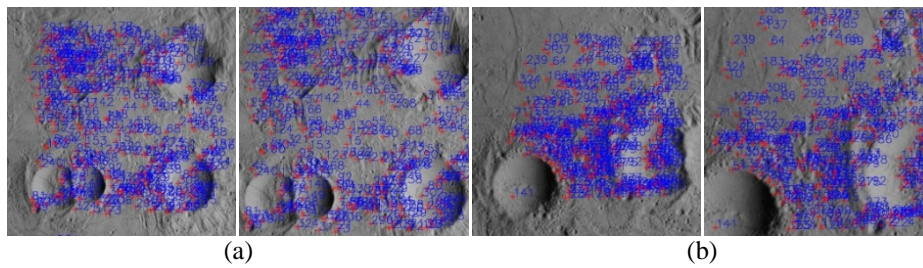


Figure 4 Matching Results.

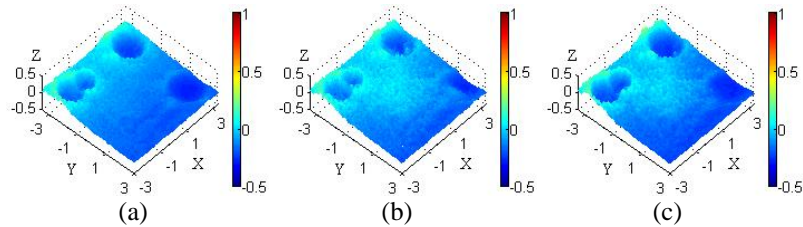


Figure 5 Reconstruction results of Image 1.

Based on the matching results of the feature points, the initial terrain can be obtained by solving Eq. (12). Then, we can use the proposed optimization methods to optimize the initial terrain. Figure 5(a) shows the scan result of the coverage area of Image 1 obtained by the FARO 3D laser scanner. Figure 5(b) shows the terrain constructed by using the quasi-dense matching method. Figure 5(c) shows the optimized terrain after optimization using the proposed method.

Figure 6(a) shows the scan result of the coverage area of Image 3. Figure 6(b) shows the terrain constructed using the quasi-dense matching method. Figure 6(c) shows the optimized terrain.

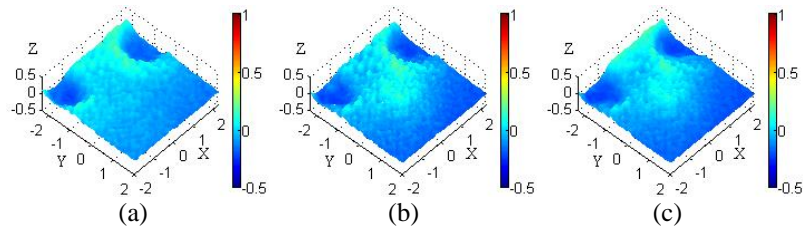


Figure 6 Reconstruction results of Image 3.

After comparing the true values of the respective scanners, the reconstruction errors of the terrain reconstructed using the quasi-dense matching method and our proposed method could be acquired. Figures 7 and 8 show the reconstruction errors of Images 1 and 3, respectively, where (a) illustrates the recovery errors of the quasi-dense matching method, and (b) illustrates the errors of our proposed method.

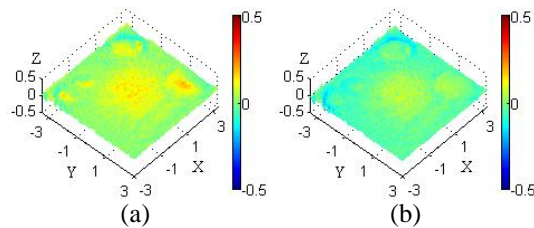


Figure 7 Reconstruction errors of Image 1.

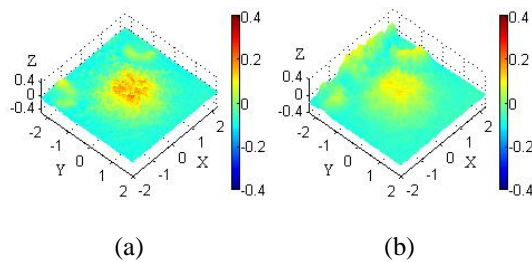


Figure 8 Reconstruction errors of Image 3.

Tables 1 and 2 show the statistical results of the reconstruction errors of Images 1 and 3, respectively.

Table 1 Error Statistics of Image 1.

Algorithm	Minimum	Maximum	Mean	Mean square
Quasi-dense matching method	-0.168	0.223	0.052	0.036
Proposed method	-0.163	0.103	0.043	0.03

Table 2 Error Statistics of Image 3.

Algorithm	Minimum	Maximum	Mean	Mean square
Quasi-dense matching method	-0.14	0.3	0.063	0.033
Proposed method	-0.129	0.141	0.052	0.024

According to the statistical results and errors shown in Figures 7 and 8, we can draw the following conclusions:

1. Considering the presence of texture-deficient and texture-repeat areas in lunar images, feature points with high precision could be obtained using the Forstner feature extraction method and could provide high-precision data for subsequent terrain reconstruction.
2. With the matching constraint of the proposed method, fewer mismatches were observed in the results. The correctness of the matching results was improved, which provides a reliable basis for terrain reconstruction.
3. The initial terrain could be constructed by using the feature points obtained using the quasi-dense matching method. The effect was better in the texture-rich area, whereas the result was poor in the shadow and texture-deficient areas.
4. The reconstruction error of our proposed method was smaller than that of the terrain constructed using the quasi-dense matching method. Our reconstructed terrains were closer to the actual situation, particularly in the area with poor texture. After optimization, the error of our method was evidently less than the initial reconstruction error. This finding shows that the proposed optimization method is feasible and can also provide reliable basic data for scientific investigation by the Chang'e III rover.
5. Several systematic errors in the terrain constructed by using the quasi-dense matching method and our proposed method were observed. In the area near the center of the image, errors in both results were large. In the area far from the center of the image, errors in both results were small. This finding is mainly due to the increase in intersection angle from the image center to the edge.
6. Several errors in the illumination direction, reflection coefficient of the lunar surface, and other parameters led to errors in the reflection model equations and resulted in the presence of certain errors in the overall final result.

7. A certain degree of similarity between the reconstruction errors of the quasi-dense matching method and our proposed method was observed. The final reconstruction accuracy of the proposed method was also determined on the basis of the accuracy of the initial terrain constructed by the feature points.

3.2 Descent Images of Chang'e III

Descent images of Chang'e III were selected to complete the reconstruction of the rover's landing area. The selected images were divided into two groups, based on the capture height. The capture heights of Images 5 and 6 are close and the capture heights of Images 7 and 8 are close. Images 5 to 8 are shown in Figures 9(a), 9(b), 9(c), and 9(d), respectively. Image 5 was taken at a height of 139.5 m, Image 6 at 136.5 m, Image 7 at 60.0 m, and Image 8 at 48.5 m. The calculated illumination directions were $(-0.9, 1, 0.8)$.

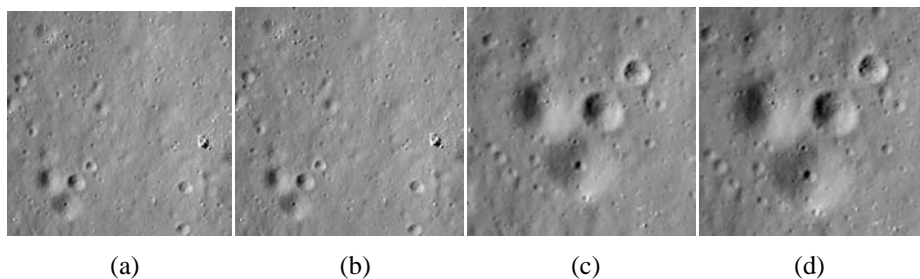


Figure 9 Descent images of Chang'e III.

First, Forstner feature point extraction of the two images with a small coverage was conducted. Then, point matching was conducted using the proposed method. To facilitate viewing, the sparse matching results are displayed in Figure 10. Figure 10(a) shows the sparse matching result of Images 5 and 6. Figure 10(b) shows the sparse matching result of Images 7 and 8.

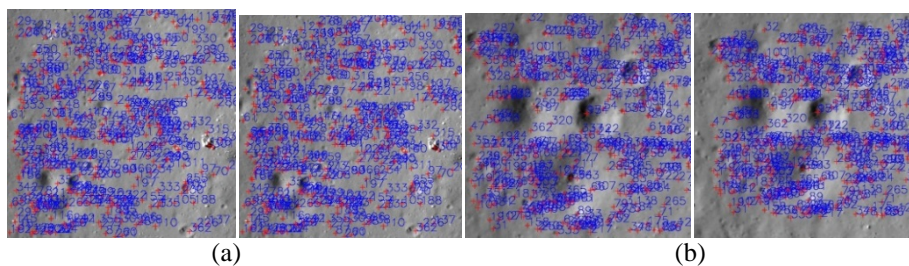


Figure 10 Matching results.

The initial terrain can be constructed by using the matching feature points and can be optimized by using the proposed method. Figure 11(a) shows the terrain of the coverage area of Image 5, which was reconstructed by using the quasi-dense matching method. Figure 11(b) shows the optimized terrain. Figure 12(a) shows the terrain of the coverage area of Image 7, which was reconstructed by using the quasi-dense matching method. Figure 12(b) shows the optimized terrain.

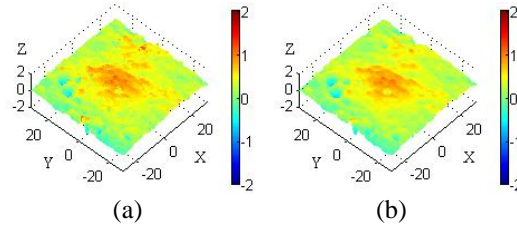


Figure 11 Reconstruction results of Image 5.

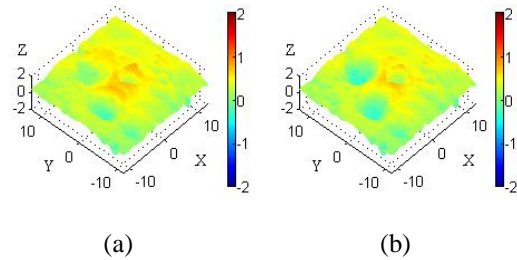


Figure 12 Reconstruction results of Image 7.

The results shown in Figures 11 and 12 reveal that the optimized terrain is closer to the actual situation. However, we also observed several systematic errors in the results of both methods.

3.3 Analysis

Considering the texture characteristic of the lunar image, mismatches occur more often in the result of traditional dense matching, which affects the reliability of the final reconstruction. Although the number of mismatches in traditional feature matching is smaller, mismatches in the texture-repeat region still exist. Therefore, the traditional method cannot meet the needs of the scientific expedition mission of Chang'e III. The proposed method first considers the feature points and then uses the geometric model of the descent process as the constraint. Finally, the surface reflection model is used to optimize the normal vectors. Therefore, the terrain is closer to the real situation. The reconstruction results obtained by the proposed method are better than

those obtained by the quasi-dense matching method, particularly in the texture-repeat and texture-deficient area.

However, the optimization algorithm results in several errors. The main factors that affect the performance of the optimization algorithm are as follows:

1. Forstner feature point extraction and the proposed geometric model constraints are used for feature matching and provide initial data with high accuracy for the ultimate terrain reconstruction. Although several errors can be eliminated by using the lens distortion parameters, several errors cannot be eliminated, which leads to matching errors.
2. Linearized collinear equations are used to solve the ground 3D coordinates of the feature points. The different positions of the matching points result in differences in the intersection angles between matching points, which leads to certain systematic errors in the solution process. This error is associated with the ground point location. The closer the point to the image center, the greater the system error. The system error is small when the point is far from the image center.
3. The normal vector of each point is obtained using the initial terrain. Taking the normal vector as the center, the new vector changes with a small step size around the normal vector. Thus, a new set of gray values can be obtained on the basis of the reflection model. The new vector is recorded when the calculated gray value is closest to the gray value of the original image. However, given the fact that several differences exist between the ideal model and the actual situation, several errors were observed in the optimized vectors.
4. The proposed optimization can only be achieved on the basis of the initial terrain obtained by feature matching. The reconstruction errors in the proposed method are similar to those in the initial terrain to a certain extent. The performance of the proposed method is better than that of the feature matching method.

4 Conclusion

This study presents a new optimized approach for terrain reconstruction of descent images. First, feature point extraction is conducted. Then, the geometric model of the time of descent image acquisition is established. The obtained geometric constraints are used instead of the traditional feature matching process. Thus, all feature points can be preserved and provide a good foundation for the reconstruction of the initial terrain. The initial terrain is constructed by solving the collinear equations. Then, the normal vector of each point is obtained. Based on the Lommel-Seeliger reflection model, the normal vectors of all the points can be optimized. Finally, terrain optimization is completed after

iteration of the normal vector field. Geometric constraints are used instead of the traditional feature matching process in order to overcome the adverse effects of the fact that the number of matching points is reduced after the traditional feature matching. It also compensates for the shortcomings of the traditional feature point matching, in which the obtained terrain is rough. Finally, geometric constraints have been successfully applied to terrain reconstruction of the landing area of Chang'e III. The experimental results showed that the accuracy of the proposed method in reconstructing the laboratory image was better than that of the traditional feature matching method. For the Chang'e III descent images, the optimized results were closer to the real situation. This finding provides a technical reference for future lunar exploration and other deep space exploration. Given that several errors still exist in the matching constraint model, the reflection model, and other factors, which lead to several errors in the reconstruction results, further research will be conducted in the future to improve accuracy.

Acknowledgements

This work was supported by the National Natural Science Foundation of China (No. 41401535), the Surveying and Mapping Basic Research Program of the National Administration of Surveying, Mapping and Geoinformation (12-01-05), and the College Student Innovation and Entrepreneurship Training Program (No. 201410147016).

References

- [1] Jia, Y., Liu, S.C., Li, M.L., Li, Q.Z., Peng, S., Weng, B., Ma, Y.Q. & Zhang, S., *Chang'E-3 System Pinpoint Landing Localization Based on Descent Image Sequence*, Chinese Science Bulletin (Chinese Version), **59**(19), pp. 1838-1843, 2014.
- [2] Sun, Z.Z., Jia, Y. & Zhang, H., *Technological Advancements and Promotion Roles of Chang'E-3 Lunar Probe Mission*, SCIENCE CHINA Technological Sciences, **56**(11), pp. 2702-2708, 2013.
- [3] Ma, Y.Q., Liu, S.C., Jia, Y., Jia, Y.H., Zhang, J.L., Wei, S.Y., Li, Q.Z., Xu, X.C., Wu, K. & Wen, B., *Experimental Research of Navigation and Localization Algorithm Based on Stereo Images for the Lunar Rover*, SCIENCE CHINA Technologica, **44**(10), pp. 1097-1104, 2014.
- [4] Ma, Y.Q., Jia, Y.H., Liu, S.C. & Jia, Y., *Bundle Adjustment Based on LM Algorithm for Rover Navigation and Localization*, Journal of Northeastern University (Natural Science), **35**(4), pp. 489-493, 2014.
- [5] Wu, W.R., Zhou, J.L., Wang, B.F. & Liu, C.K., *Key Technologies in the Teleoperation of Chang'E-3" Jade Rabbit" Rover*, SCIENCE CHINA Informations, **44** (4), pp. 425-440, 2014.

- [6] Liu, B., Xu, B., Liu, Z.Q., Liu, Y.L., Di, K.C., Tang, G.S. & Zhou, J.L., *Descending and Landing Trajectory Recovery of Chang'e-3 Lander Using Descent Images*, Journal of Remote Sensing, **18**(5), pp. 981-987, 2014.
- [7] Ni, D., Chui, Y.P., Qu, Y., Yang, X., Qin, J., Wong, T.T., Ho, S.S.H. & Heng, P.A., *Reconstruction of Volumetric Ultrasound Panorama Based on Improved 3D SIFT*, Computerized Medical Imaging and Graphics, **33**(7), pp.559-566, 2009.
- [8] Bulatov, D., Wernerus, P. & Heipke, C., *Multi-view Dense Matching Supported by Triangular Meshes*, Journal of Photogrammetry and Remote Sensing, **66**(6), pp. 907-918, 2011.
- [9] Xue, X.L., Meng, C. & Jia, Y., *An Improved Method for Terrain Mapping from Descent Images*, Advances in Intelligent and Soft Computing, **122**, pp. 547-555, 2012.
- [10] Shin, D. & Muller, J.P., *Progressively Weighted Affine Adaptive Correlation Matching for Quasi-Dense 3D Reconstruction*, Pattern Recognition, **45**(10), pp. 3795-3809, 2012.
- [11] Ahmadabadian, A.H., Robson, S., Boehm, J., Shortis, M., Wenzel, K. & Fritsch, D., *A Comparison of Dense Matching Algorithms for Scaled Surface Reconstruction Using Stereo Camera Rigs*, Journal of Photogrammetry and Remote Sensing, **78**(4), pp. 157-167, 2013.
- [12] Dellepiane, M., Dell'Unto, N., Callieri, M., Lindgren, S. & Scopigno, R., *Archeological Excavation Monitoring Using Dense Stereo Matching Techniques*, Journal of Cultural Heritage, **14**(3), pp.201-210, 2013.
- [13] Meng, C., Zhou, N., Xue, X.L. & Jia, Y., *Homography-based Depth Recovery with Descent Images*, Machine Vision and Applications, **24**(5), pp. 1093-1106, 2013.
- [14] Joglekar, J., Gedam, S.S. & Mohan, B.K., *Image Matching Using SIFT Features and Relaxation Labeling Technique—a Constraint Initializing Method for Dense Stereo Matching*, IEEE Transactions on Geoscience and Remote Sensing, **52**(9), pp. 5643-5652, 2014.
- [15] Nebiker, S., Lack, N. & Deuber, M., *Building Change Detection from Historical Aerial Photographs Using Dense Image Matching and Object-Based Image Analysis*, Remote Sensing, **6**(9), pp. 8310-8336, 2014.
- [16] Stentoumis, C., Grammatikopoulos, L., Kalisperakis, I. & Karras, G., *On Accurate Dense Stereo-Matching Using a Local Adaptive Multi-Cost Approach*, Journal of Photogrammetry and Remote Sensing, **91**(5), pp. 29-49, 2014.
- [17] Meng, C., Zhou, N. & Jia, Y., *Improved Best Match Search Method in Depth Recovery with Descent Images*, Machine Vision and Applications, **26**(2-3), pp. 251-266, 2015.
- [18] Koutsoudisa, A., Ioannakis, G., Vidmar, B., Arnaoutoglou, F. & Chamzas, C., *Using Noise Function-based Patterns to Enhance Photogrammetric*

- 3D Reconstruction Performance of Featureless Surfaces*, Journal of Cultural Heritage, **16**(5), pp. 664-670, 2015.
- [19] Liu, J., Li, C.P., Fan, X.F. & Wang, Z.Q., *Reliable Fusion of Stereo Matching and Depth Sensor for High Quality Dense Depth Maps*, Sensors, **15**(8), pp. 20894-20924, 2015.
- [20] Chen, C.C. & Hsieh, S.L., *Using Binarization and Hashing for Efficient SIFT Matching*, Journal of Visual Communication and Image Representation, **30**(6), pp. 86-93, 2015.
- [21] Ouellet, J.N. & Hebert, P., *Precise Ellipse Estimation without Contour Point Extraction*, Machine Vision and Applications, **21**(9), pp. 59-67, 2009.
- [22] McEwen, A., *A Precise Lunar Photometric Function*, Lunar and Planetary Science, **27**(3), pp. 841-842, 1996.
- [23] Kreslavsky, M.A., Shkuratov, Y.G., Velikodsky, Y.I., Kaydash, V.G., Stankevich, D.G. & Pieters, C.M., *Photometric Properties of the Lunar Surface Derived from Clementine Observations*, Journal of Geophysical Research, **105**(E8), pp.281-295, 2000.